

Machine learning approach for ion imprinted (IIP) and non-imprinted (NIP) polymer discrimination based on pyrolysis kinetic data

Jéssica de Vasconcelos Cardoso Barros^{a,1}, João Daniel Santos Castro^{a,b,1},
 Cesário Francisco das Virgens^{a,*}

^a Universidade do Estado da Bahia, Departamento de Ciências Exatas e da Terra, Programa de Pós-Graduação em Química Aplicada, CEP 41150-000, Salvador, BA, Brazil

^b Zhejiang University, State Key Laboratory of Clean Energy Utilization, Institute of Thermal Power Engineering, 310027, Hangzhou, PR China

ARTICLE INFO

Keywords:

Ion imprinted polymers
 Machine learning
 Kinetic study
 Pyrolysis
 Thermal decomposition

ABSTRACT

The improper disposal of effluents containing toxic elements, such as nickel and mercury, can result in the gradual deterioration of surface water quality, impacting aquatic ecosystems and human health. Ionically imprinted polymers (IIPs) are promising candidates for remediating toxic areas due to their high removal rates and selectivity. In this study, multifunctional IIPs were developed using Ni²⁺ and Hg²⁺ as template ions and dithizone, methacrylic acid, and ethylene glycol dimethacrylate as complexing agent, monomer, and cross-linking agent, respectively, to remove Ni (II) and Hg (II) from effluents. The thermal decomposition behavior and degradation mechanism of ion imprinted polymers were investigated to address the issue of limited lifespan. The kinetic study revealed that the samples showed significant thermal stability, and the IIP-Duo sample exhibited higher activation energy compared to the non-imprinted polymer (NIP) and the mono-imprinted polymer (IIP), indicating that double impression alters the structure of the polymer and consequently its thermal degradation. Three machine learning models were applied to classify the samples according to imprinting, successfully predicting 95% or more of the classes correctly without overfitting or overmodelling. The master plot method showed that imprinting did not affect the thermal decomposition pathway, with the IIP, IIP-Duo, and NIP samples presenting the same mechanism geometrical contraction model (R3) at a conversion rate between 0.4 and 0.9. These findings suggest that multifunctional IIPs are promising materials for remediating areas impacted by toxic elements.

1. Introduction

Environmental concerns related to water have become increasingly relevant with the rapid growth of the global economy and the accelerated pace of industrialization. These factors have created difficulties with the supply of clean drinking water and the adequate recycling of wastewater, leading to a deterioration of surface water quality. (Yusof et al., 2019). Despite intense governmental regulations aimed at regulating the release of industrial wastewater, heavy metals from these discharges can potentially contaminate surface water resources. It is important to continue enforcing regulations and implementing measures to prevent such contamination and protect water quality [1].

According to the World Health Organization (WHO), toxic bio-accumulation metals, such as nickel, lead, mercury, and cadmium are

listed as top priority contaminants, once it presents high toxicity even at low concentrations, causing several damages to the environment and the living beings [2]. For instance, the presence of nickel in water is attributed to the leaching of rocks and sediments in addition to the disposal of effluents from battery and electroplating industries [3,4]. High concentrations of nickel can lead to serious health problems, such as dermatitis, kidney and lung damage, and can also favor the production of cancer cells [5,6]. The World Health Organization (WHO) has established a concentration limit of 20 µg/L of total nickel in drinking water [2,7].

On the other hand, mercury is widely used in the manufacturing process of various products including lamps, batteries, and dental fillings. It can be released into the environment due to natural occurrences such as volcanic eruptions and mineral degradation, causing pollution of

* Corresponding author.

E-mail address: cvirgens@uneb.br (C.F. Virgens).

¹ These authors contributed to the work equally and should be regarded as first co-authors.

water, soil, and air [8,9]. Its main anthropogenic sources are related to waste from thermoelectric power plants, chlorine and alkali plants, dental amalgam, and incineration of medical and household waste. Due to its high level of toxicity and bioaccumulation in the ecosystem, the World Health Organization (WHO) has set a maximum concentration of 10 µg/L of mercury in wastewater and a maximum allowable limit of 1 µg/L in drinking water [2,10].

In this context, several studies in recent years have been the target of investigation in the search for a route to remove these contaminants present in effluents, among them there are: liquid-liquid extraction [11], adsorption [12], chemical precipitation, coagulation, ion exchange and reverse osmosis. However, these techniques often result in the generation of secondary waste, making them inefficient [13–16]. To tackle this issue, Ion Imprinted Polymers (IIP) have emerged as a promising technique, due to the generation of materials with high selectivity, low cost, and ease of preparation [17–19]. These materials are synthesized to promote selectivity and ion recognition, which is advantageous for analyzing low concentrations and ultra-trace levels [20–23].

The synthesis of IIP, through the Bulk method, occurs through the reaction of a functional monomer, a cross-linking agent, a radical initiator, and a template ion. This process occurs in three steps: (i) - formation of a complex between the metal ion of interest (template ion) and the monomer; (ii) - polymerization, to incorporate the metal ion of interest into the polymeric network or the linear polymer; and finally occurs (iii) - the removal of the template ion to generate the selective cavity in the polymer [24,25]. It is also possible to add simultaneously two template ions [26–28] to remove selectively more ions or ionic species in the reaction medium.

Once the IIP's are mainly used as a high functional and selective adsorbent, this type of materials has also a short life cycle, once the adsorption capacity tends to decay after successive adsorption-desorption cycles. An old-fashioned way to dispose these materials is dumping in landfills or even its incineration [29]. These strategies can impact significantly the environment, since these materials are loaded with toxic metals, carcinogenic compounds and/or other harmful substances precursors [30,31]. The components loaded in the adsorbent can also alter the thermal decomposition and possible mechanisms associated with the incineration/pyrolysis of these materials [32]. The kinetic modelling of the decomposition plays a crucial role for the better comprehension of these materials' behavior under different work conditions [33].

In recent years, the use of isoconversional methods such as Flynn-Wall-Ozawa (FWO) [34,35] and Distributed Activation Energy Method (DAEM) [36] has gained increasing attention due to their versatility in modeling various complex solid-state reaction systems, including biomass [37–39], co-pyrolysis systems (biomass + plastics) [40,41] and conventional polymeric materials as PET [42], Poly(lactic Acid) (PLA) [43], PVC [30], polyurethane [39] and polystyrene [44]. While conventional pyrolysis and catalytic pyrolysis of polymeric materials have been widely studied, particularly for plastics and waste plastics, there is a lack of literature concerning the thermal stability, mechanisms, and kinetics of imprinted polymers thermal decomposition. Understanding the physicochemical characteristics of imprinted polymers is essential for their appropriate utilization and safe disposal as a new material. To improve the evaluation and interpretation of pyrolysis features, machine learning and/or chemometrics tools can be utilized [45]. However, the use of machine learning algorithms to model or predict pyrolytic characteristics of polymers remains limited in the literature [46–49], particularly for imprinted polymers. The present work aims to synthesize, characterize, and evaluate the pyrolysis behavior of polymers based on methylacrylic acid (MAA) for the selective removal of Ni(II) and/or Hg(II) ions. The influence of the amount of monomer and double/mono/non-imprinting methodologies was also analyzed to reduce synthesis time and reagent consumption. Furthermore, to better understand the kinetics of the chain polymerization/depolymerization reaction and aspects related to the decomposition of these polymers, the

thermal stability and pyrolysis kinetic parameters were analyzed using DAEM and FWO methodologies. Based on the kinetic data, three different machine learning classification algorithms, support vector machine, logistic regression, and Adaboost, were evaluated to better understand the influence of imprinting methodologies on pyrolysis characteristics.

2. Experimental

2.1. Reagents and solutions

All reagents used in the synthesis of IIP were of analytical grade. Methacrylic acid (MAA), 2,2'-azo-isobutyronitrile (AIBN), 98% ethylene glycol dimethacrylate (EGDMA) all from Sigma-Aldrich, 99.5% mercury (II) chloride, 99.5% nickel (II) chloride, 99.7% dimethyl sulfoxide (DMSO) and ethanol PA from Vetec (Rio de Janeiro, RJ, Brazil), 98% 1,5-diphenylthiocarbazon (Fluka), acetonitrile (ACN) for HPLC, gradient grade, ≥99.9% and hydrochloric acid (HCl) from Merck and ultrapure water obtained from a model OS10LX water purification system (Gehaka®, São Paulo, SP, Brazil). The hydrochloric acid solutions were prepared by diluting with ultrapure water.

2.2. Characterization

2.2.1. Infrared spectroscopy

A Fourier transform infrared spectrometer model FT-IR Spectrum 100 (PerkinElmer, Germany) was used to obtain the attenuated total reflectance (ATR) spectrum in the infrared region from 4000 to 600 cm⁻¹ with 16 scans per sample.

2.2.2. Thermal analysis

The obtained materials were characterized by thermogravimetric analysis coupled with differential thermal analysis (TG-DTA) using a thermogravimetric analyzer model TG-60 (Shimadzu), mass 8 mg ± 0.01 mg, heating rate of 5, 10 and 15 °C min⁻¹, in a nitrogen atmosphere with a flow rate of 50 mL min⁻¹, in a platinum crucible.

2.3. Polymer synthesis

2.3.1. IIP - double ion imprinted (Ni²⁺/Hg²⁺)

The followed methodology agrees with the one proposed by Lins [50]. In this work, the synthesis was optimized by reducing the amount of monomer and increasing the heating temperature from 80 °C to 100 °C.

In a rounded bottom glass flask (100 mL) it was dissolved, with rapid stirring, 0.2 mmol of 1,5-diphenylthiocarbazon (Dithizone-(HDz)) in a mixture of solvents (1:1) ACN/DMSO for 10 min in order to have total solubilization of the dithizone. Then 0.05 mmol of mercury (II) chloride and 0.05 mmol of nickel (II) chloride were added to the mixture, stirred for another 30 min to form the mercury (II) dithizonate (Hg(HDz)₂) and nickel (II) dithizonate (Ni(HDz)₂) complexes. Subsequently, while maintaining stirring, 32 mmol of MAA, 64 mmol of EGDMA, and 0.08 mmol of AIBN were added, in that order. Immediately an ultrapure 99.9 % nitrogen gas purge was performed inside the glass flask in order to remove the oxygen released in the synthesis. It was then sealed and placed in an oil bath at 100 °C. The polymerization of IIP occurred in 17 min, obtaining a brown solid named IIP-Hg/Ni. The solid obtained was dried in an oven at 80 °C for 2 h, macerated and sieved at 80 mesh.

The removal of the template ion was performed with hydrochloric acid (HCl), varying concentrations from 0.5 to 1.5 mol L⁻¹, being stirred for 30 min on a shaking table. After stirring, it was filtered and read in the Flame Atomic Absorption Spectrophotometer to check if the template ion was completely removed. All tests were performed three times.

2.3.2. NIP - (non-imprinted polymer) and IIP - ion imprinted polymer (Ni²⁺)

The same methodology as mentioned before was employed for this

synthesis, however for the IIP Ni²⁺ was used only the nickel (II) chloride as ion template. For the NIP synthesis there is no addition of ion template, furthermore the polymer was dried using a rotary evaporator in the following conditions: rotation 40 rpm, temperature 60 °C.

2.3.3. Template ion leaching

The determination of Hg²⁺ ions was performed using the Atomic Fluorescence Spectrometer model LUMINA 3300 (Aurora instruments, Canada), A hollow cathode lamp (HCL) was used for all the mercury measurements using the wavelength at 253.6 nm, current of 30 mA, PMT of 360 V.

The determination of Ni²⁺ was performed using Flame Atomic Absorption Spectrophotometer, model: SensAA Dual, (GBC Scientific) with wavelength at 232.0 nm, current of 4.0 mA and deuterium lamp for background radiation correction.

2.4. Distributed activated energy model (DAEM)

The DAEM methodology considers first-order irreversible and parallel reactions, each with its own frequency factor called the Arrhenius pre-exponential factor (A) and activation energy. This model requires at least three experimental datasets, which can be obtained at different heating rates (β) using thermogravimetric analysis [51,52]. According with this model, developed by Miura & Maki, all frequency factors (A) differ only in activation energy, and the quantity of independent reactions is large enough to allow for a continuous Gaussian distribution of activation energy. Hence, a Double-Gaussian model was developed, as described by the equation below [53–55].

$$\ln\left(\frac{\beta}{T^2}\right) = -\frac{E_a}{RT} + \ln\left(\frac{A R}{E_a}\right) + 0.6075 \quad (1)$$

where:

β is the heating rate (in K min⁻¹);

A is the pre-exponential factor;

R is the universal gas constant;

E_a the activation energy (in kJ mol⁻¹);

T is the temperature in K.

Using a graph of $\ln\beta/T^2$ vs. $1/T$ the kinetic parameters can be obtained.

2.5. Flynn-Wall-Ozawa (FWO) isoconversional method

The kinetic parameters of the thermal decomposition of the printed polymers were determined using the Flynn-Wall-Ozawa (FWO) method [38], which is derived from Doyle's approximation for the Arrhenius equation [56]. The data obtained from thermogravimetric analysis were analyzed using the Ozawa's method equation, which can be written in its logarithmic form as follows

$$\ln(\beta) = \ln\left(\frac{A E_a}{g(\alpha) R}\right) - 5.331 - \left(1.052 \cdot \frac{E_a}{R T}\right) \quad (2)$$

where:

β is the heating rate (in K min⁻¹);

A is the pre-exponential factor;

R is the universal gas constant;

E_a the activation energy (in kJ mol⁻¹);

T is the temperature in K.

The parameters of the Arrhenius equation, such as activation energy and pre-exponential factor, can be determined graphically using the $\ln\beta$ vs. $1/T$ plot. The slope of the straight line found in the plot provides the activation energy, while the linear coefficient yields the pre-exponential factor.

2.6. Artificial intelligence approach

For the artificial intelligence approach, kinetic data from both DAEM and FWO kinetic methods were used as input, including the mean temperature for each fraction (α). Each step of thermal decomposition with α between 0.25 and 0.9 (excluding solvents and water evaporation) was evaluated as a single dataset with 7 features. The datasets were then classified according to their specifications (imprinted, double-imprinted, and non-imprinted) using the scheme presented below.

2.6.1. Machine learning algorithms

All machine learning algorithms were implemented using the Scikit-learn package from the Orange software (version 3.25). Orange [57] is a Python-based visual programming software that enables the implementation of predetermined machine learning algorithms. Users can adjust the algorithms' parameters to suit specific data needs.

2.6.1.1. Support vector machine. The type of algorithm used was Support Vector Machine (SVM) with the following parameters: Cost regression (c) = 1.0, Regression loss epsilon (ϵ) = 0.1, Kernel type RBF, and numerical tolerance = 0.001.

SVM was first proposed by Vapnick [58] and works by mapping the original data points to a high-dimensional space where the classification problem becomes simpler. The mapping is done by choosing a suitable kernel function [59].

2.6.1.2. Adaboost. The machine learning algorithm used in this project was Adaboost with a tree base estimator. The algorithm employed 50 estimators, a learning rate of 1.0, and a linear regression loss function.

Adaboost was first proposed by Freund & Schapire [60] and focuses on solving the most difficult classification problem in the dataset using an algorithm as the base estimator. The base estimator is employed successively by the Adaboost algorithm, setting different weights during each test round. At the end of each round, the base estimator outputs a hypothesis that is evaluated by the algorithm, and the weights are redistributed to minimize classification errors. After the training process is complete, Adaboost combines all the intermediate hypotheses to create one final hypothesis in a sequential ensemble method.

2.6.1.3. Logistic regression. In this project, logistic regression was used with Lasso regularization (L1) and a regularization strength of C = 1. The Lasso regularization method is applied to improve the prediction accuracy and interpretability of regression models [61]. Logistic regression is a statistical method that estimates the probability of an event occurring based on the dataset training input by combining one or more independent variables linearly. Its main goal is to find the decision boundaries among the classes and provides probability as a response [62].

2.6.2. Algorithm validation and verification

All classification models in this project were trained using the data and validated using the k-fold cross-validation methodology (k = 10). The validation method involved dividing the dataset into k parts, of which k-1 parts were used for modeling (training), and the remaining part was reserved for testing. The dataset was tested ten times, with each test using a different fold.

To evaluate and compare the classification models generated by the different algorithms, a confusion matrix was used [63]. The confusion matrix is a table that shows the actual classes in the horizontal lines and the predicted classes in the columns. It provides a detailed evaluation of the algorithm's accuracy, identifying false positives, false negatives, true positives, and true negatives during the prediction process.

The Rank feature algorithm from Scikit-learn Python package [64] was applied to evaluate the classification results based on the features. This was used to select the most important three features that contribute

to the classification, using different scoring methods such as information gain, gain ratio, Gini, ANOVA, Chi2, ReliefF, and Fast Correlation Based Filter (FBCF).

2.7. Master plot method

Criado's method [65,66] was applied to accurately determine the mechanism of polymeric solid-state reaction. The method is defined by a function:

$$Z(\alpha) = \frac{d\alpha/dt}{\beta} \pi(x)T \quad (3)$$

where $x = \frac{Ea}{RT}$ and $\pi(x)$ are an approximation of the temperature integral, which cannot be expressed in simplicity. In this study, the Senum - Yang approximation was used, which presents errors lower than $10^{-5}\%$ when $x > 20$ [67].

Experimental curve $Z(\alpha)$ is defined by Poletto [68] as:

$$Z(\alpha) = \frac{d\alpha}{dt} \frac{Ea}{R} \frac{e^{\frac{Ea}{RT}}}{e^{\frac{Ea}{RT}}} P(x) \quad (4)$$

Being $P(x)$ the expression of the fourth rational of Senum - Yang [67]:

$$P(x) = \frac{e^{-x}}{x} \cdot \frac{x^3 + 18x^2 + 86x + 96}{x^4 + 20x^3 + 120x^2 + 240x + 120} \quad (5)$$

where $x = Ea/RT$

Master plot as a function of the conversion factor (α) can be obtained according to the following equation:

$$Z(\alpha) = f(\alpha) \cdot g(\alpha) \quad (6)$$

Since $f(\alpha)$ and $g(\alpha)$ are different solid-state reaction models.

In order to increase the precision in the estimation of the degradation mechanism of the samples, the features selected previously on section 2.7, from the best suitable kinetic method for the classification, were used in equations (4) and (5).

To increase the precision in the determination of the decomposition mechanism, the present work uses the Criado's method modification proposed by Castro and collaborators [45], that proposes the use of the

algebraic equation derived from the Pythagorean Theorem, to measure the distance between two points in a Cartesian plane, since the x axis is shared by both experimental and master curves (see Fig. 1).

3. Results and discussion

3.1. Fourier transform infrared spectrometry (FTIR)

The spectra obtained (Fig. 2) of the NIP, IIP-Ni²⁺ and IIP-Ni²⁺/Hg²⁺ samples present great similarities, differing only in the intensity of the absorptions, displacements of some bands between the imprinted polymers and the non-imprinted polymer. Such results are consistent with the results obtained by Lins [50], indicating that the polymer structure remained similar. The experimental spectra were also compared with the monomer spectra (Methacrylic Acid), found at Spectral Database for Organic Compounds (SDBS) [69].

On the NIP sample, is observed a very discrete hydroxyl band referring to the MAA monomer, as can be seen in Fig. 3. This possibly occurs as a consequence of inter/intramolecular hydrogen bonds in the polymer chain, but a wide and not very intense band is observed between 3600 and 3300 cm⁻¹ in samples IIP-Ni²⁺ and IIP-Ni²⁺/Hg²⁺, which may also be related to the presence of hydroxyl (-OH) due to moisture absorption, that can be associated with the sample storage.

In region I of Fig. 2, range 3060-2830 cm⁻¹, we note the presence of weak absorptions that are attributed to stretching of C_{sp}³-H and C_{sp}²-H bonds. In this spectra region, the NIP sample presents lower intensity, if compared with the other samples. The main reason for this phenomenon is related to the specific surface area ratio, once according Planinšek [70], the particle size and the specific surface area directly influence the absorption and reflectance.

The region II that corresponds to the absorption in the range of 1720 cm⁻¹, is associated with the C=O stretching, that in this case refers to the carbonyl band present in the methacrylic acid (monomer), as observed in polymers synthesized using the same monomer, cross-linking agent and radical initiator. On the reference monomer spectra (Methacrylic Acid, MAA) [69], this carbonyl band is at 1697 cm⁻¹, indicating that after polymerization the band was displaced, being strong evidence that there was consumption of MAA during the synthesis [71,72]. Next to this band, in region III of Fig. 2, there is a weak

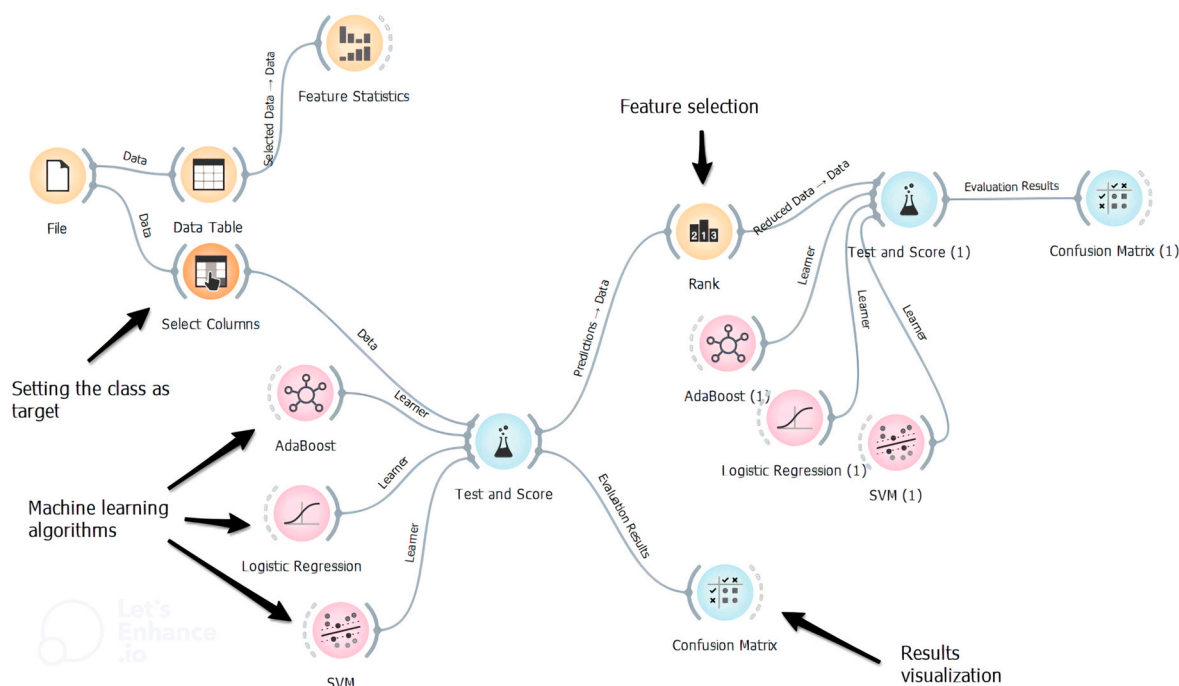


Fig. 1. Artificial intelligence approach for thermal degradation prediction (art done by the author).

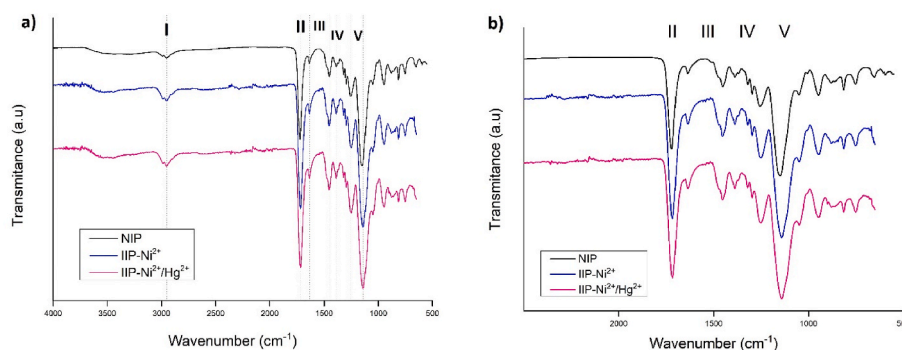


Fig. 2. Infrared spectra by Attenuated Total Reflection (FTIR-ATR) of the samples NIP, IIP-Ni²⁺ and IIP-Ni²⁺/Hg²⁺ (a) 4000 to 500 cm⁻¹ and (b) 2500 to 500 cm⁻¹.

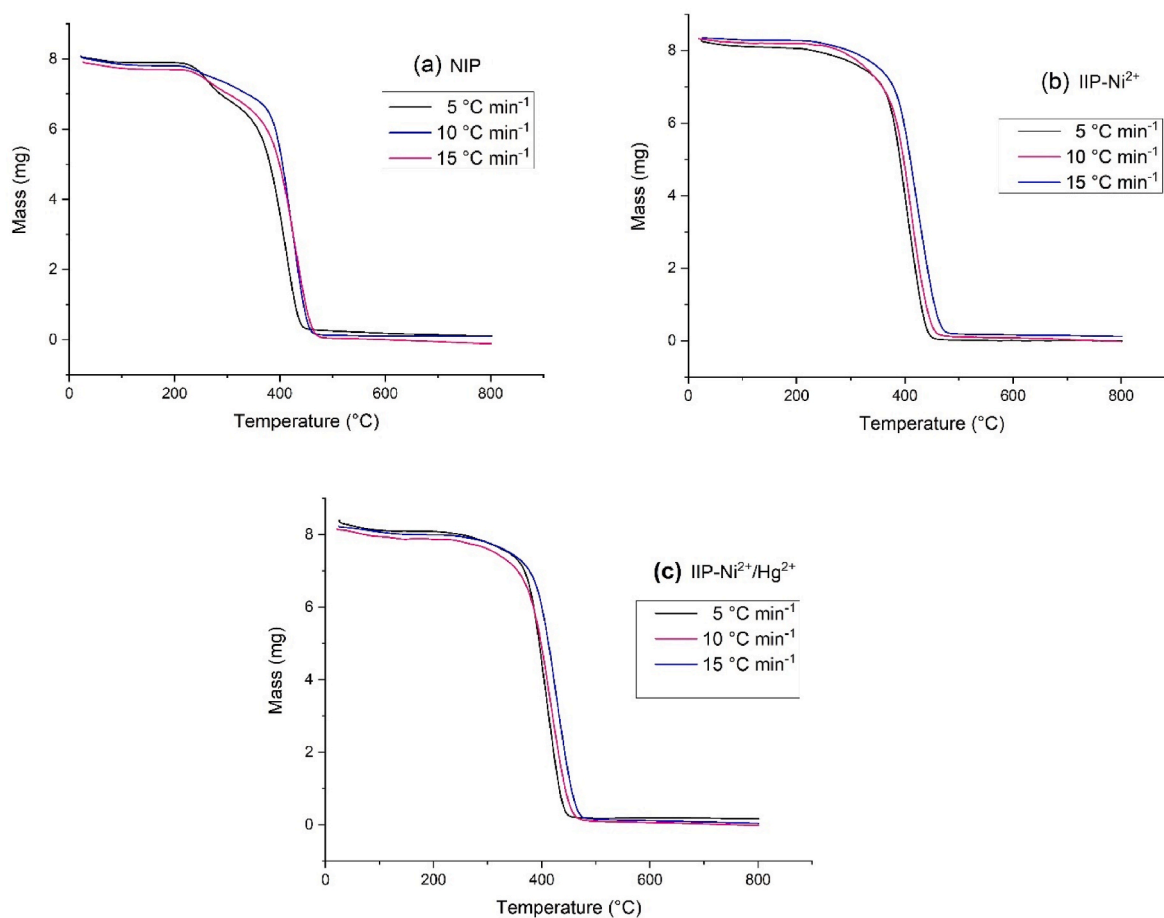


Fig. 3. Thermogravimetric curves at heating rates of 5, 10 and 15 °C min⁻¹ of (a) NIP; (b) IIP-Ni²⁺ and (c) IIP-Ni²⁺/Hg²⁺.

C=C stretching band at 1636 cm⁻¹ (for all three samples), while in the reference spectra [69] the band associated to the vinyl group appears intense. Other bands in the region from 3000 to 2600 cm⁻¹, which are present in the spectrum of MAA [69] also do not appear in the produced polymers, confirming that there was complete polymerization of the MAA molecule to form the polymer chain (Yusof et al., 2019).

The absorptions in the range of 1455 and 1388 cm⁻¹, observed in the region (IV) of Fig. 2, are attributed to CH₂ and CH₃ folding, respectively. In region (V), the bands between 1256 and 1142 cm⁻¹ are C–O bond stretching, characteristic of ester, referring to ethylene glycol dimethacrylate [39]. The spectra of the printed polymers, IIP-Ni²⁺ and IIP-Ni²⁺/Hg²⁺, present equal bands with the same intensity, which shows that the simultaneous printing does not interfere in the formation of the polymer chain, since the metal is incorporated into the ligand to

form a template before reacting with the monomer.

Table 1 summarizes the bands found on the imprinted polymers according to the regions previously described.

3.2. Thermogravimetric analysis

The profiles of the TGA curves for imprinted and non-imprinted polymers, shown in Fig. 3, are similar. Analyzing the TG curves and the DTG curves (Fig. 4), is noticed the existence of a main mass loss event, between 201.5 and 498.6 °C for NIP, 209–507 °C for IIP-Ni²⁺ and between 215.2 and 514.7 °C for IIP-Ni²⁺/Hg²⁺, totaling a mass loss of 96.29%, 96.94% and 96.35% respectively. From 500 °C onwards, it is observed that there is practically no mass variation.

In the first stage, between 50 and 150 °C, there is a very low mass loss

Table 1

Main bands and its respective absorptions observed in FTIR spectra for NIP, IIP-Ni²⁺ and IIP-Ni²⁺/Hg²⁺ samples.

Region	Bands	Wavenumber (cm ⁻¹)		
		NIP	IIP-Ni ²⁺	IIP-Ni ²⁺ /Hg ²⁺
I	νC_{sp}^3-H e C_{sp}^2-H	3045–2840	3060–2840	3060–2830
II	$\nu C=O$	1722	1718	1717
III	$\nu C=C$	1636	1636	1636
IV	CH_2 and CH_3 folding	1452 and	1455 and	1455 and
		1388	1388	1388
V	$\nu C-O$	1256 and	1250 and	1250 and
		1148	1142	1142

associated with the evaporation of water and other volatile solvents used in the synthesis. The fact that the mass loss is quite subtle indicates that there is little solvent and water residue, because the polymers were dried properly, as evidenced by the FTIR results (Fig. 2); the second event has greater mass loss and is related to the decomposition of the polymer chain, between 200 and 514 °C, approximately. A shorter decomposition interval in single-event curves, represents a greater the thermal stability of the material when heated [54,73,74].

The analysis of the TGA graphs at heating rates of 5, 10 and 15 min⁻¹ show a shift in the region of maximum thermal decomposition to higher temperatures when the heating rate is increased, as shown in Fig. 3. This phenomenon is associated with hysteresis, which causes an increase in the temperature gradient within the sample [74–76].

As evidenced in the DTG (Fig. 4), the temperature at which the mass loss velocity shows a maximum value is 417.6 °C for IIP-Ni²⁺ and at 425.8 °C for the IIP-Ni²⁺/Hg²⁺ sample and 266.3 and 430.2 °C for the NIP, indicating that first a slower reaction occurs and then a second reaction happens faster for the NIP. There is a slight mass loss over 500 °C and it is associated with the end of mercury dithizonate complexes and nickel dithizonate complexes inside of the polymeric chains [77].

3.3. Kinetic study

The kinetic parameters obtained in FWO and DAEM methods for each sample are summarized in the kinetic table data (Supplementary material) and graphed in Fig. 5.

As can be observed in Fig. 5, the main decomposition event is related to the beginning of the depolymerization step of the sample. This event is also observed in the DTG curve (Fig. 4) and starts before the conversion range $\alpha = 0.1$, for the IIP-Ni²⁺ and IIP-Ni²⁺/Hg²⁺ imprinted polymers, at 209.0 and 215.2 °C respectively.

For the FWO method, the highest activation energies are observed at 203.88, 214.26 and 219.82 kJ mol⁻¹ for NIP, IIP-Ni²⁺ and IIP-Ni²⁺/Hg²⁺, respectively, at different conversion ranges (α), which is common in decomposition of complex matrix samples, as polymers [78,79].

Both methods show an increasing curve in activation energy (Ea) for the samples IIP-Ni²⁺ and IIP-Ni²⁺/Hg²⁺, while for the NIP, in the conversion ranges 0.05 to 0.25 shows a decrease in Ea values, which is evidenced by the correlation coefficient R², in the kinetic table (supplementary material), below 0.9000. These coefficients are low for the three samples in the conversion ranges cited. In this sense, for further evaluations only the conversion range (α) between 0.25 and 0.9 was employed.

The values of the activation energies (Ea) of the imprinted polymers are close to and higher than the values obtained for the non-imprinted polymer. This corroborates that NIP has less stable structure than IIPs due to the absence of the template ion during synthesis [28,80,81].

It is observed that in the conversion range from 0.25 to 0.90, the Ea values for the IIPs are close in both methods, averaging 207 kJ mol⁻¹ (FWO) and 218 kJ mol⁻¹ (DAEM) close for the IIP-Ni²⁺ sample. However, for the IIP-Ni²⁺/Hg²⁺ sample the conversion range that shows a low variation of Ea ranging from 0.30 to 0.90 and have an average of 215 kJ mol⁻¹ (FWO) and 226.41 kJ mol⁻¹ (DAEM). At the initial α , the IIP-Ni²⁺/Hg²⁺ sample shows higher Ea values in both methods (72.3 kJ

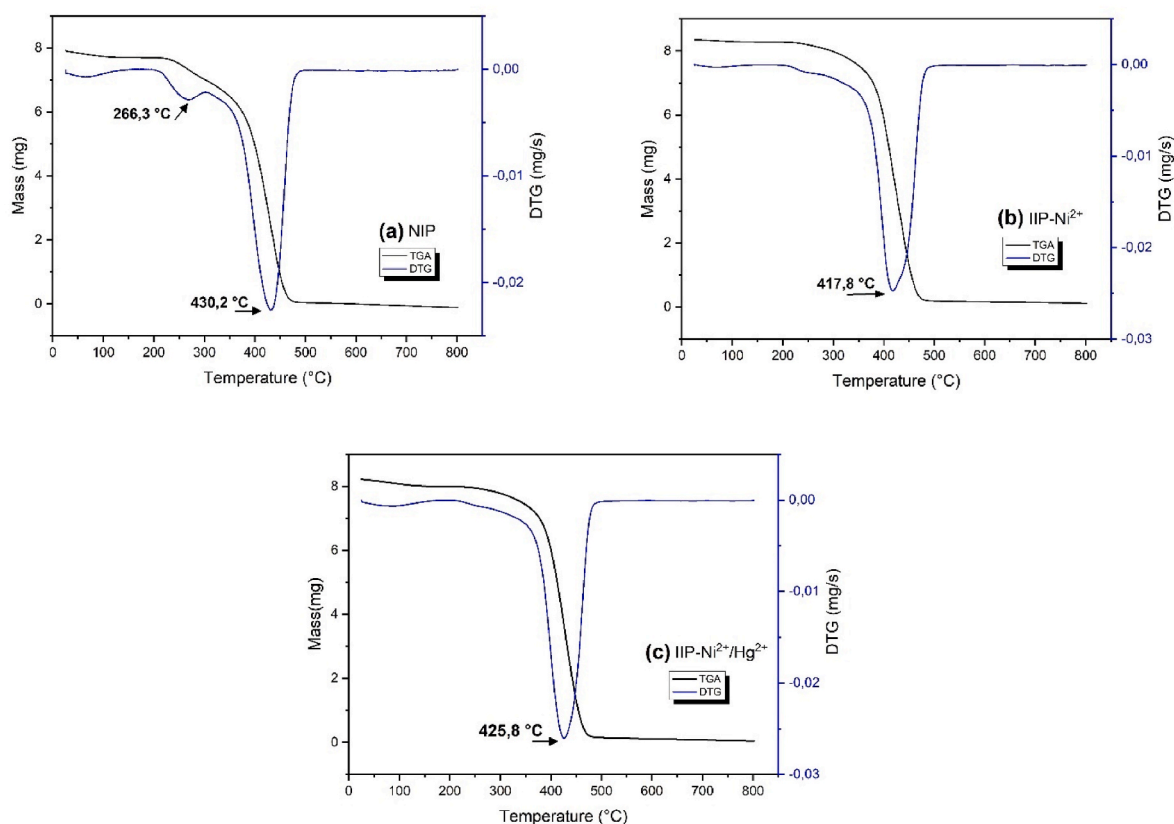


Fig. 4. TG thermogravimetric curves and their derivatives at a heating rate of 15 °C min⁻¹ of (a) NIP; (b) IIP-Ni²⁺ and (c) IIP-Ni²⁺/Hg²⁺.

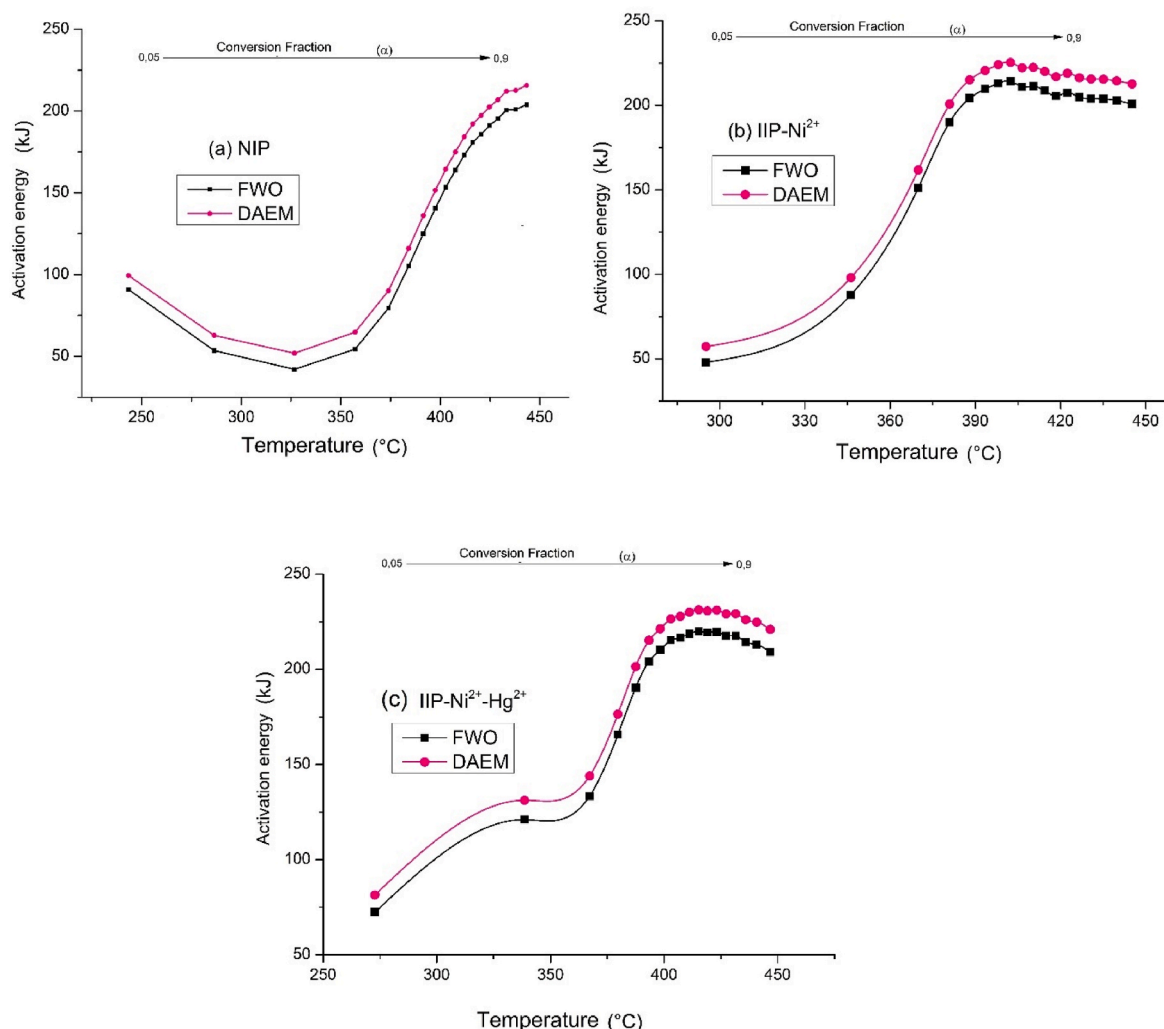


Fig. 5. Activation energy graph (obtained by FWO and DAEM methods) as function of temperature: (a) NIP; (b) IIP-Ni²⁺ and (c) IIP-Ni²⁺/Hg²⁺.

mol⁻¹ in FWO and 81.4 kJ mol⁻¹ in DAEM), compared to the other samples. The Ea values continue to increase until $\alpha = 0.9$, at approximately 450 °C, indicating that the decomposition of the polymer chain occurs gradually. The variation of Ea values is consistent with what is expected for complex polymeric samples, which do not present a well-defined decomposition kinetics, as is the case with ion-printed polymers [82,83].

It is also observed that the ionic imprinting (with one or two template ions) influences the decomposition kinetics of the polymers obtained, since the Ea values of the IIP-Ni²⁺ sample present thermal stability (according with results in both methods), varying little between $\alpha = 0.30$ to 0.90, with a graphical profile with low slope, similar to a horizontal straight line. On the other hand, the IIP-Ni²⁺/Hg²⁺ sample presents increasing values in this same range, resulting in a curvilinear graphical profile, as observed in Fig. 5. The NIP sample presents an increasing curve, without a plateau of constant Ea [45].

According to Mortezaeikia and collaborators, an apparently constant value of Ea over a certain conversion range indicates that decomposition occurs through a single step, while gradual and significant changes in Ea are indications of a change in the overall decomposition mechanism, corroborating what is evidenced by the TG/DTG curve [52,79].

Although the IIP-Ni²⁺/Hg²⁺ sample presents higher activation energy values in the two analyzed methods, as we can observe in Table 4, double imprinting does not confer higher thermal stability to the material, because with α between 0.05 and 0.90, the temperature range for the IIP-Ni²⁺/Hg²⁺ sample is 272.7–446.7 °C, while for the IIP-Ni²⁺ this

temperature range goes from 295.1 to 445.2 °C, presenting a ΔT lower than the range of the IIP-Ni²⁺/Hg²⁺ sample. According to Mothé, the smaller the range of the initial and final decomposition temperature, the more stable the material is for thermal decomposition [74].

For better data visualization, a heatmap containing the kinetic triplet (normalized data) from both FWO and DAEM methods was built as shown in Fig. 6. In general, the values of activation energy for the non-imprinted polymer (NIP) are lower compared to the imprinted samples. The pre-exponential factor ($\ln A$) and reaction velocity rate ($\ln K$) also have lower values than IIP-Duo and IIP. Through the heatmap visualization, a pattern can be observed in the kinetic data: NIP < IIP < IIP-Duo. In the kinetic data table (supplementary material), the R² values of the lines for obtaining Ea are shown, and it is observed that both methods are suitable for the thermokinetic behavior modelling of the samples.

The degradation of the complex formed between the ligand (dithizone) and the mold ions, which was only observed as a discrete event in the TG curve (Fig. 3), does not appear in the kinetic study because it occurs at temperatures above 500 °C, beyond the range of degradation (α) analyzed (0.05–0.9) [77].

3.4. Assessment of machine learning algorithms

The classification results can be properly evaluated using a confusion matrix, a square matrix (GxG) whose rows and columns are associated with actual data and predictions respectively [84].

Table 2
Distances between master plot theoretical models and experimental curves for NIP sample.

	A2	A3	A4	R1	R2	R3	D1	D2	D3	D4	F1	F2	F3	L2
0,25	0,306	0205	0,148	0451	0,243	0157	0,544	0727	0,754	0157	0,536	0284	0,506	0257
0,3	0,248	0164	0,119	0366	0,191	0122	0,483	0638	0,670	0126	0,451	0251	0,455	0231
0,35	0,188	0123	0,089	0276	0,140	0089	0,398	0520	0,556	0096	0,355	0207	0,385	0190
0,4	0,127	0082	0,059	0185	0,091	0057	0,288	0376	0,409	0066	0,248	0152	0,291	0137
0,45	0,064	0041	0,029	0093	0,044	0027	0,155	0203	0,226	0034	0,130	0084	0,166	0073
0,5	0,000	0000	0,000	0000	0,000	0000	0,000	0000	0,000	0000	0,000	0000	0,000	0000
0,55	0,067	0042	0,029	0093	0,042	0026	0,178	0236	0,277	0037	0,145	0104	0,228	0081
0,6	0,137	0085	0,059	0187	0,083	0050	0,377	0509	0,615	0076	0,309	0237	0,550	0170
0,65	0,212	0129	0,090	0281	0,121	0072	0,599	0823	1030	0,118	0496	0,410	1022	0,265
0,7	0,293	0177	0,123	0375	0,158	0094	0,841	1183	1542	0,162	0712	0,642	1753	0,365
0,75	0,383	0229	0,158	0469	0,194	0113	1105	1598	2186	0,210	0969	0,969	2969	0,471
0,8	0,486	0287	0,197	0562	0,227	0132	1390	2079	3013	0,260	1284	1462	5212	0,582
0,85	0,610	0354	0,242	0655	0,259	0149	1697	2641	4117	0,315	1692	2289	10,067	0,697
0,9	0,770	0440	0,298	0748	0,289	0164	2024	3313	5694	0,372	2270	3948	23,948	0,817

Table 3
Distances between master plot theoretical models and experimental curves for IIP sample.

	A2	A3	A4	R1	R2	R3	D1	D2	D3	D4	F1	F2	F3	L2
0,25	0,323	0221	0,165	0467	0,260	0174	0,544	0744	0,771	0140	0,552	0301	0,523	0240
0,3	0,258	0174	0,128	0375	0,201	0132	0,483	0647	0,680	0116	0,461	0261	0,465	0221
0,35	0,194	0129	0,094	0282	0,145	0094	0,398	0526	0,562	0091	0,361	0213	0,390	0185
0,4	0,130	0085	0,062	0188	0,094	0060	0,288	0379	0,412	0063	0,251	0155	0,294	0134
0,45	0,066	0042	0,031	0094	0,046	0029	0,155	0204	0,227	0033	0,132	0085	0,168	0072
0,5	0,000	0000	0,000	0000	0,000	0000	0,000	0000	0,000	0000	0,000	0000	0,000	0000
0,55	0,067	0042	0,030	0094	0,043	0026	0,178	0237	0,277	0036	0,146	0105	0,229	0081
0,6	0,138	0086	0,061	0188	0,084	0051	0,377	0510	0,616	0075	0,310	0238	0,551	0169
0,65	0,213	0131	0,092	0282	0,123	0074	0,599	0824	1031	0,116	0497	0,411	1023	0,263
0,7	0,294	0178	0,124	0376	0,159	0095	0,841	1184	1544	0,161	0713	0,643	1754	0,364
0,75	0,384	0230	0,159	0470	0,195	0115	1105	1600	2188	0,208	0970	0,970	2970	0,470
0,8	0,488	0288	0,198	0564	0,229	0133	1390	2080	3014	0,259	1286	1464	5214	0,580
0,85	0,611	0356	0,243	0657	0,261	0150	1697	2642	4118	0,313	1694	2290	10,068	0,696
0,9	0,772	0441	0,299	0749	0,291	0166	2024	3314	5696	0,371	2271	3949	23,949	0,816

Table 4
Distances between master plot theoretical models and experimental curves for IIP Duo sample.

	A2	A3	A4	R1	R2	R3	D1	D2	D3	D4	F1	F2	F3	L2
0,25	0,321	0220	0,163	0465	0,258	0172	0,544	0742	0,769	0142	0,550	0299	0,521	0242
0,3	0,257	0173	0,127	0374	0,199	0131	0,483	0646	0,679	0117	0,459	0260	0,464	0222
0,35	0,193	0128	0,093	0281	0,145	0093	0,398	0525	0,561	0092	0,360	0212	0,389	0185
0,4	0,130	0085	0,061	0188	0,094	0060	0,288	0379	0,412	0063	0,251	0155	0,294	0134
0,45	0,065	0042	0,030	0094	0,045	0029	0,155	0204	0,227	0033	0,132	0085	0,168	0072
0,5	0,000	0000	0,000	0000	0,000	0000	0,000	0000	0,000	0000	0,000	0000	0,000	0000
0,55	0,067	0042	0,030	0094	0,043	0026	0,178	0237	0,277	0036	0,146	0105	0,229	0081
0,6	0,138	0086	0,061	0188	0,084	0051	0,377	0510	0,616	0074	0,310	0238	0,551	0169
0,65	0,213	0131	0,092	0282	0,123	0074	0,599	0824	1031	0,116	0497	0,411	1023	0,263
0,7	0,294	0179	0,124	0376	0,160	0095	0,841	1185	1544	0,161	0713	0,643	1754	0,364
0,75	0,385	0230	0,160	0470	0,195	0115	1105	1600	2188	0,208	0970	0,970	2970	0,469
0,8	0,488	0288	0,198	0564	0,229	0133	1390	2080	3014	0,259	1286	1464	5214	0,580
0,85	0,611	0356	0,243	0657	0,261	0150	1697	2642	4118	0,313	1694	2290	10,068	0,696
0,9	0,771	0440	0,298	0748	0,290	0164	2024	3313	5694	0,372	2270	3948	23,948	0,817

According to the confusion matrix analysis shown in Fig. 7, the Adaboost algorithm correctly classified the imprinted and non-imprinted polymers with 100% accuracy, compared to 97.8% and 95.8% for the SVM and Logistic Regression algorithms, respectively. The strong performance of the Adaboost algorithm in classification can be attributed to its nature: the train data is divided and a model is created for each split of the dataset. These intermediate models are assigned weights according to their accuracy, and are then added together to create the final model, which is a strategic approach to increase the overall accuracy of classification [85]. It is also important to note that overfitting was not observed during classification using this algorithm. Overfitting occurs when a model fits the training data well but is inefficient in predicting new results or includes more features than necessary for prediction [86]. To properly evaluate if the model overfit the dataset, insignificant features were removed from the model training according to the rank shown in Fig. 8, and a new model was generated.

The efficiency and accuracy metrics for the prediction model did not change significantly after the removal of these insignificant features.

Additionally, cross-validation was employed to further evaluate the generated model. This validation method involves testing the model on unseen data (data that the model has not learned before) using the k-fold methodology [87], where the dataset was split into 10 folds. Nine folds were used to train the algorithm, and the remaining fold was used to test the model [45].

Fig. 8 shows that both the class distribution and the number of features per class are balanced, and there is no missing data. This is important because imbalanced datasets can significantly degrade algorithm performance, reducing overall accuracy and leading to misclassification of minority class samples or treating them as data noise. Therefore, having a balanced dataset is crucial for accurate decision-making [88].

The SVM and Logistic Regression algorithms misclassified the final

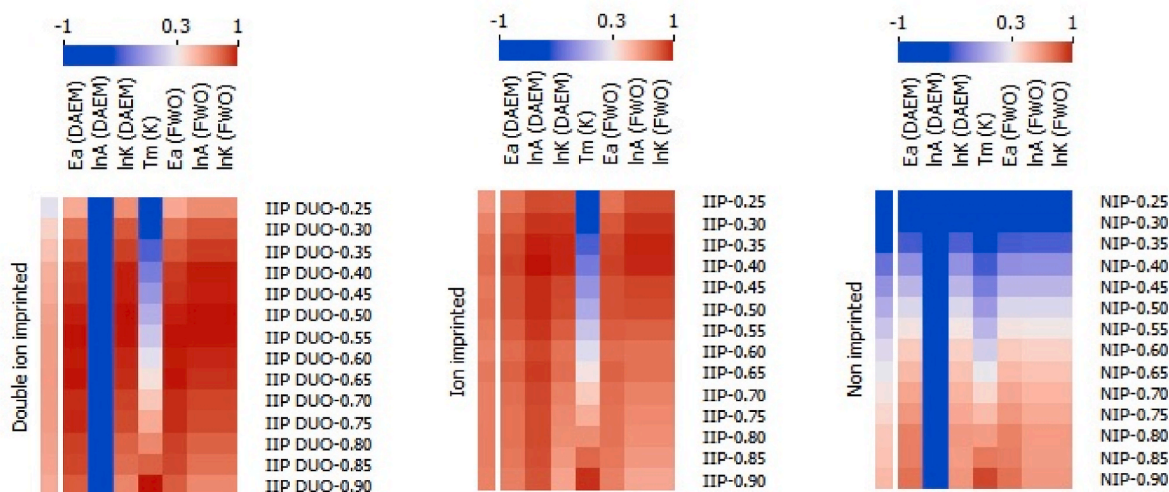


Fig. 6. Heat map analysis of kinetic triplets (lnA, Ea and lnK for IIP Double, IIP and NIP).



Fig. 7. Confusion matrix for predicted classification between different machine learning algorithms (a) Adaboost; (b) Logistic Regression and (c) Support Vector Machine (SVM).

and/or initial stage ($\alpha = 0.25$ and/or 0.9) of the double ion imprinted decomposition as a non-imprinted polymer. These polymers are produced from the polymerization of methacrylic acid (MAA) and dithizone. This misclassification can be attributed to a region where there is no relationship between any monomer in the polymeric chain next to the ion complex during thermal decomposition.

Fig. 9 shows the ranking of features (variables) that contribute to better classification of polymers. According to the figure, the kinetic triplet from the Distributed Activation Energy Model (DAEM) is the most suitable for machine learning classification prediction of imprinted and non-imprinted polymers. This can be attributed to the nature of the DAEM, as it is well adapted for complex pyrolysis reactions and is able to describe kinetic parameters over a wide range of temperatures and heating rates [89]. Additionally, the method has shown good results when modelling the thermal decomposition of polymers [39].

3.5. Master plot method

Fig. 10 illustrates the thermal decomposition mechanism for the polymer samples (NIP, IIP, and IIP Duo) in the $\alpha = 0.25$ to 0.9 range, which covers the process of thermal degradation/depolymerization of the polymeric chain in a solid-state in a nitrogen atmosphere. In this figure, the straight lines in black represent the experimental curve of the polymers, where each point relates to a specific decomposition stage of

the solid (α). The overlap between the points of the black line and the points of a theoretical curve determines the experimental solid-state mechanism of the data.

Tables 2–4 provide a summary of the distances between each point of the experimental sample and theoretical mechanism sample, according to the methodology proposed by Castro and collaborators [45]. The tables highlight the mechanism that shows the minimum distance compared to each master plot. The combined analysis of the graph and the table reveals that there is a complex multistep mechanism occurring during the pyrolysis of NIP, IIP, and IIP Duo.

The initial stage ($\alpha = 0.25$ – 0.3) of the thermal decomposition of the NIP sample (Non-imprinted polymer) is associated with the Avrami-Erofeyev mechanism (A4), which is related to nucleation and growth. This mechanism has also been reported for polystyrene in a nitrogen atmosphere [44].

According to the master plot analysis (Fig. 9, Table 3 and 4), the polymer chain decomposition for imprinted polymers (IIP and IIP Duo) occurs following two different mechanisms.

1. For α between 0.25 and 0.35 , the processes are associated with a Ginstling-Brounshtein mechanism (D4), a deceleratory diffusion model that describes the decrease of the reaction rate with reaction progress [90]. The volatiles evolution reactions during the polymer degradation are related to diffusion models since these processes are



Fig. 8. Feature and class distribution: Non imprinted polymer (green); Ion imprinted (blue); Double Ion imprinted (red)

	#	Info. gain	Gain ratio	Gini	ANOVA	χ^2	Relieff	FCBF
1	N InA (DAEM)	1.127	0.564	0.445	7200.075	28.719	0.615	1.697
2	N Ea (DAEM)	0.833	0.417	0.353	18.665	21.594	0.074	0.869
3	N InK (DAEM)	0.741	0.371	0.284	21.893	22.625	0.070	0.000
4	N InK (FWO)	0.741	0.371	0.284	22.072	22.625	0.071	0.000
5	N InA (FWO)	0.741	0.371	0.284	22.072	22.625	0.071	0.000
6	N Ea (FWO)	0.731	0.366	0.294	18.875	20.656	0.074	0.000
7	N Tm (K)	0.013	0.007	0.006	0.252	0.125	0.007	0.000

Fig. 9. Feature ranking for the proper classification of the samples.

controlled by the diffusive escape of gases but still have a solid barrier that slows down the reaction rate [91].

- For α between 0.35 and 0.9, the mechanism observed is a R3 model, a phase boundary-controlled reaction (contracting volume). The R3 mechanism assumes that nucleation occurs quickly on the surface of the solid, and the rate of degradation is controlled by the resulting interaction surface towards the solid core [90,92]. A similar pattern of thermal decomposition mechanism, a D-type mechanism followed by an R-type, was also found when modelling the polylactic acid polymer decomposition [43].

It is also important to note that the three samples, NIP, IIP, and IIP Duo, with α between 0.4 and 0.9 show the same degradation mechanism, R3, revealing that the polymer ion-imprinting does not affect the thermal decomposition mechanism in this range.

4. Conclusions

This work describes the use of machine learning algorithms to classify imprinted and non-imprinted polymers based on pyrolysis kinetic data obtained using the Distributed Activation Energy Method (DAEM) and Flynn-Wal-Ozawa Method. Additionally, the chemical structure, thermal decomposition, and pyrolysis mechanisms associated with ion-imprinted and non-imprinted polymers were evaluated.

Ionic imprinted polymers were synthesized, including an IIP with one template ion (IIP-Ni²⁺) and a bifunctional IIP with two template ions (IIP-Ni²⁺/Hg²⁺, or IIP-Duo). Comparing the FTIR spectra of the monomer and all the samples indicated that all the monomer was consumed during the synthesis to form the polymer chain.

The thermogravimetric (TG) curves of the polymers show a similar and single main mass loss event, occurring between 201.5 and 498.6 °C for NIP, 209–507 °C for IIP-Ni²⁺, and 215.2–514.7 °C for IIP-Ni²⁺/Hg²⁺, which is mainly associated with thermal depolymerization. Beyond 500 °C, there is practically no mass variation.

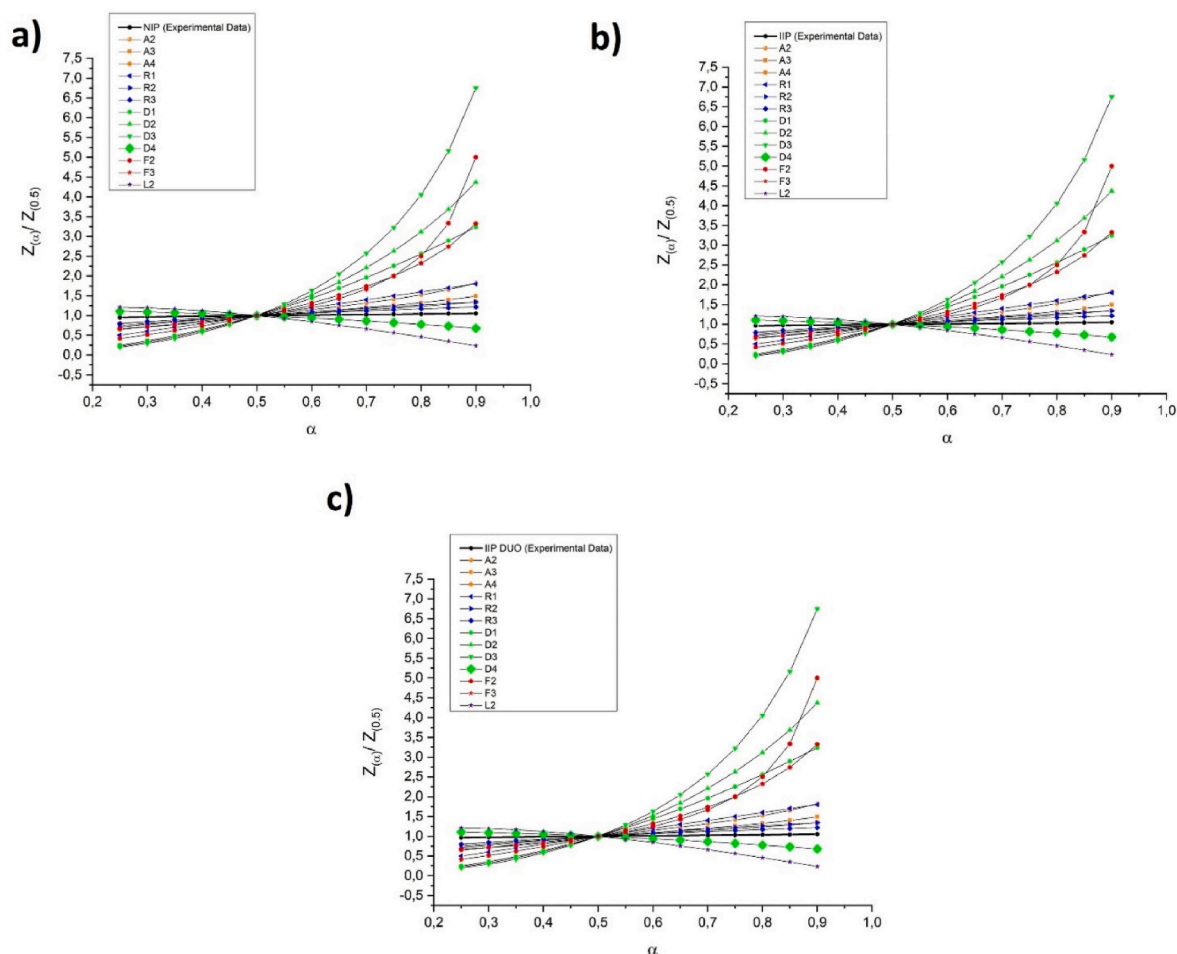


Fig. 10. Master curves and experimental data obtained using the Criado method for: a) NIP sample; b) IIP sample and c) IIP Duo sample.

The kinetic study is consistent with other studies on samples of complex polymeric matrix, with the R^2 values indicating the methods are suitable for the samples. It is also observed that ionic imprinting, with one or two template ions, influences the decomposition kinetics of the polymers obtained. The E_a values of the IIP-Ni²⁺ sample show thermal stability, as indicated by results from both kinetic methods, with little variation between $\alpha = 0.30$ and 0.90 . On the other hand, the IIP-Ni²⁺/Hg²⁺ and NIP samples show increasing values in this same range.

The IIP-Ni²⁺/Hg²⁺ sample generally presents higher activation energy values, while double imprinting does not increase the thermal stability of the material, as observed by the difference of temperature range with α between 0.05 and 0.90 for both samples.

The machine learning classification of polymers revealed that the Adaboost algorithm accurately classified imprinted and non-imprinted polymers with 100% accuracy based on the kinetic data, compared to 97.8% and 95.8% for SVM and Logistic regression algorithms, respectively. Adaboost's performance can be attributed to its adaptive nature in creating small models for the whole dataset and combining them to produce a robust and reliable model.

Analysis of the master plot shows that the polymer chain decomposition for imprinted polymers (IIP and IIP Duo) occurs through two different mechanisms: (I) with α between 0.25 and 0.35 associated with a deceleratory diffusion model (D4), and (II) with α between 0.35 and 0.9 , a phase boundary-controlled reaction (contracting volume), an R3 model. It is important to note that all three samples (NIP, IIP, and IIP Duo) with α between 0.4 and 0.9 exhibit the same degradation mechanism, R3, indicating that polymer ion-imprinting does not affect the thermal decomposition mechanism in this range.

Further evaluations are necessary to analyze the amount and type of gases released during the pyrolytic process, as well as check for any potential release of toxic metals during this stage.

Statements and declarations

- ✓ A scholarship was received from Fundação de Amparo à Pesquisa do Estado da Bahia – FAPESB, via Master's Scholarship between 2020 and 2022, for Jéssica de Vasconcelos Cardoso Barros;
- ✓ Partial financial support was received from CAPES, via Master's Scholarship between 2018 and 2019, for João Daniel S. Castro
- ✓ All authors certify that they have no affiliations with or involvement in any organization or entity with any financial interest or non-financial interest in the subject matter or materials discussed in this manuscript.

CRedit authorship contribution statement

Jéssica de Vasconcelos Cardoso Barros: Material preparation, data collection and analysis were performed, The first draft of the manuscript was written, all authors commented on previous versions of the manuscript, All authors read and approved the final manuscript. **João Daniel Santos Castro:** Material preparation, data collection and analysis were performed, The first draft of the manuscript was written. **Cesário Francisco das Virgens:** Material preparation, data collection and analysis were performed, All authors contributed to the study conception and design, all authors commented on previous versions of the manuscript, All authors read and approved the final manuscript.

Declaration of competing interest

The authors declare there is no financial interests/personal relationships which may be considered as potential competing interests.

Data availability

All the data used is on supplementary material

Acknowledgements

The authors thank the funding agencies FAPESB and China Scholarship Council (CSC) for granting the scholarship and the post-graduation program PGQA (UNEB) for the infrastructure provided.

References

- [1] T. Lekkoba, F. Ntuli, T. Falayi, Application of coal fly ash for treatment of wastewater containing a binary mixture of copper and nickel, *J. Water Proc. Eng.* (2020), <https://doi.org/10.1016/j.jwpe.2020.101822>.
- [2] WHO Guidelines for Drinking-Water Quality: Incorporating 1st and 2nd Addenda. Recommendations. World Health Organization 2008, vol. 1.
- [3] S.S. Moersidik, R. Nugroho, M. Handayani, Kamilawati, M.A. Pratama, Optimization and reaction kinetics on the removal of nickel and COD from wastewater from electroplating industry using electrocoagulation and advanced oxidation processes, *Heliyon* 6 (2020), e03319, <https://doi.org/10.1016/j.heliyon.2020.e03319>.
- [4] W. Meouche, K. Laatikainen, A. Margailan, T. Silvonen, H. Siren, T. Sainio, I. Beurroies, R. Denoyel, C. Branger, Effect of porogen solvent on the properties of nickel ion imprinted polymer materials prepared by inverse suspension polymerization, *Eur. Polym. J.* 87 (2017) 124–135, <https://doi.org/10.1016/j.eurpolymj.2016.12.022>.
- [5] J. He, H. Shang, X. Zhang, X. Sun, Synthesis and application of ion imprinting polymer coated magnetic multi-walled carbon nanotubes for selective adsorption of nickel ion, *Appl. Surf. Sci.* 428 (2018) 110–117, <https://doi.org/10.1016/j.apsusc.2017.09.123>.
- [6] N.H. Elsayed, A. Alatawi, M. Monier, Diacetylmonoxine modified chitosan derived ion-imprinted polymer for selective solid-phase extraction of nickel (II) ions, *React. Funct. Polym.* 151 (2020), 104570, <https://doi.org/10.1016/j.reactfunctpolym.2020.104570>.
- [7] C. Wang, T. Li, G. Yu, S. Deng, Removal of low concentrations of nickel ions in electroplating wastewater by combination of electro dialysis and electrodeposition, *Chemosphere* 263 (2021), 128208, <https://doi.org/10.1016/j.chemosphere.2020.128208>.
- [8] H. Albatrni, H. Qiblawey, M.H. El-Naas, Comparative study between adsorption and membrane technologies for the removal of mercury, *Sep. Purif. Technol.* 257 (2021), 117833, <https://doi.org/10.1016/j.seppur.2020.117833>.
- [9] K.K. Jinadasa, E. Peña-Vázquez, P. Bermejo-Barrera, A. Moreda-Piñeiro, New adsorbents based on imprinted polymers and composite nanomaterials for arsenic and mercury screening/speciation: a review, *Microchem. J.* 156 (2020), 104886, <https://doi.org/10.1016/j.microc.2020.104886>.
- [10] K.A. Samad, I.S.M. Salleh, M.A.K.M. Zahari, H.W. Yusoff, Batch study on the removal of mercury (II) ion from industrial wastewater using activated palm oil fuel ash, *Mater. Today Proc.* 17 (2019) 1126–1132, <https://doi.org/10.1016/j.matpr.2019.06.536>.
- [11] Z. Gao, X. Ma, Speciation analysis of mercury in water samples using dispersive liquid-liquid microextraction combined with high-performance liquid chromatography, *Anal. Chim. Acta* 702 (2011) 50–55, <https://doi.org/10.1016/j.aca.2011.06.019>.
- [12] N.M. Marin, A. Ficai, L.A. Constantin, L. Motelica, R. Trusca, New chelate resins prepared with direct red 23 for Cd²⁺, Ni²⁺, Cu²⁺ and Pb²⁺ removal, *Polymers* 14 (2022) 5523, <https://doi.org/10.3390/polym14245523>.
- [13] J.J. Rueda-Marquez, I. Levchuk, P. Fernández Ibañez, M. Sillanpää, A critical review on application of photocatalysis for toxicity reduction of real wastewaters, *J. Clean. Prod.* 258 (2020), 120694, <https://doi.org/10.1016/j.jclepro.2020.120694>.
- [14] J. Georgieva, E. Valova, S. Armyanov, N. Philippidis, I. Poullos, S. Sotiropoulos, Bi-component semiconductor oxide photoanodes for the photoelectrocatalytic oxidation of organic solutes and vapours: a short review with emphasis to TiO₂-WO₃ photoanodes, *J. Hazard Mater.* 211–212 (2012) 30–46, <https://doi.org/10.1016/j.jhazmat.2011.11.069>.
- [15] T.A. Saleh, Trends in the sample preparation and analysis of nanomaterials as environmental contaminants, *Trends in Environmental Analytical Chemistry* 28 (2020) 1–10, <https://doi.org/10.1016/j.teac.2020.e00101>.
- [16] X. Deng, L. Lü, H. Li, F. Luo, The adsorption properties of Pb(II) and Cd(II) on functionalized graphene prepared by electrolysis method, *J. Hazard Mater.* 183 (2010) 923–930, <https://doi.org/10.1016/j.jhazmat.2010.07.117>.
- [17] Y. Huang, J.R. Du, Y. Zhang, D. Lawless, X. Feng, Removal of mercury (II) from wastewater by polyvinylamine-enhanced ultrafiltration, *Sep. Purif. Technol.* 154 (2015) 1–10, <https://doi.org/10.1016/j.seppur.2015.09.003>.
- [18] X. Zhang, H. Wang, X. Sun, H. Shang, Y. Di, Z. Zhao, Preparation and properties of thermo-sensitive surface Pb(II) ion-imprinted polymers, *Colloids Surf. A Physicochem. Eng. Asp.* 577 (2019) 138–146, <https://doi.org/10.1016/j.colsurfa.2019.05.064>.
- [19] Y. Chen, X. Ma, J. Peng, Highly selective removal and recovery of Ni(II) from aqueous solution using magnetic ion-imprinted chitosan nanoparticles, *Carbohydr. Polym.* 271 (2021), 118435, <https://doi.org/10.1016/j.carbpol.2021.118435>.
- [20] L. Chen, S. Xu, J. Li, Recent advances in molecular imprinting technology: current status, challenges and highlighted applications, *Chem. Soc. Rev.* 40 (2011) 2922, <https://doi.org/10.1039/c0cs00084a>.
- [21] F. Shakerian, K.H. Kim, E. Kwon, J.E. Szulejko, P. Kumar, S. Dadfarnia, A.M. Haji Shabani, Advanced polymeric materials: synthesis and analytical application of ion imprinted polymers as selective sorbents for solid phase extraction of metal ions, *TrAC, Trends Anal. Chem.* 83 (2016) 55–69, <https://doi.org/10.1016/j.trac.2016.08.001>.
- [22] M.S. Jagirani, A. Balouch, S.A. Mahesar, A. Kumar, A.R. Baloch, Abdullah, M. I. Bhangar, Fabrication of cadmium tagged novel ion imprinted polymer for detoxification of the toxic Cd²⁺-ion from aqueous environment, *Microchem. J.* 158 (2020), 105247, <https://doi.org/10.1016/j.microc.2020.105247>.
- [23] R. Huang, X. Ma, X. Li, L. Guo, X. Xie, M. Zhang, J. Li, A novel ion-imprinted polymer based on graphene oxide-mesoporous silica nanosheet for Fast and efficient removal of chromium (VI) from aqueous solution, *J. Colloid Interface Sci.* 514 (2018) 544–553, <https://doi.org/10.1016/j.jcis.2017.12.065>.
- [24] M. Fattahi, E. Ezzatzadeh, R. Jalilian, A. Taheri, Micro solid phase extraction of cadmium and lead on a new ion-imprinted hierarchical mesoporous polymer via dual-template method in river water and fish muscles: optimization by experimental design, *J. Hazard Mater.* 403 (2021), 123716, <https://doi.org/10.1016/j.jhazmat.2020.123716>.
- [25] S. Mishra, A. Tripathi, Selective solid phase extraction and pre-concentration of Cu (II) ions from aqueous solution using Cu(II)-ion imprinted polymeric beads, *J. Environ. Chem. Eng.* 8 (2020), 103656, <https://doi.org/10.1016/j.jece.2020.103656>.
- [26] I.M. Kenawy, M.A. Ismail, M.A.H. Hafez, M.A. Hashem, Synthesis and characterization of novel ion-imprinted guanyl-modified cellulose for selective extraction of copper ions from geological and municipality sample, *Int. J. Biol. Macromol.* 115 (2018) 625–634, <https://doi.org/10.1016/j.ijbiomac.2018.04.100>.
- [27] X. Cai, J. Li, Z. Zhang, F. Yang, R. Dong, L. Chen, Novel Pb²⁺ ion imprinted polymers based on ionic interaction via synergy of dual functional monomers for selective solid-phase extraction of Pb²⁺ in water samples, *ACS Appl. Mater. Interfaces* 6 (2014) 305–313, https://doi.org/10.1021/AM4042405.SUPPL_FILE/AM4042405_SI_001.PDF.
- [28] L. Wang, J. Li, J. Wang, X. Guo, X. Wang, J. Choo, L. Chen, Green multi-functional monomer based ion imprinted polymers for selective removal of copper ions from aqueous solution, *J. Colloid Interface Sci.* 541 (2019) 376–386, <https://doi.org/10.1016/j.jcis.2019.01.081>.
- [29] D. He, L. Zhang, Y. Zhao, Y. Mei, D. Chen, S. He, Y. Luo, Recycling spent Cr adsorbents as catalyst for eliminating methylmercaptan, *Environ. Sci. Technol.* 52 (2018) 3669–3675, <https://doi.org/10.1021/acs.est.7b06357>.
- [30] S. Honus, S. Kumagai, G. Fedorko, V. Molnár, T. Yoshioka, Pyrolysis gases produced from individual and mixed PE, PP, PS, PVC, and PET—Part I: production and physical properties, *Fuel* 221 (2018) 346–360, <https://doi.org/10.1016/j.fuel.2018.02.074>.
- [31] Y. Li, H. Yu, L. Liu, H. Yu, Application of Co-pyrolysis biochar for the adsorption and immobilization of heavy metals in contaminated environmental substrates, *J. Hazard Mater.* 420 (2021), 126655.
- [32] J. He, V. Strezov, R. Kumar, H. Weldekidan, S. Jahan, B.H. Dastjerdi, X. Zhou, T. Kan, Pyrolysis of heavy metal contaminated *Avicennia marina* biomass from phytoremediation: characterisation of biomass and pyrolysis products, *J. Clean. Prod.* 234 (2019) 1235–1245.
- [33] P.E. Sánchez-Jiménez, L.A. Pérez-Maqueda, A. Perejón, J.M. Criado, A new model for the kinetic analysis of thermal degradation of polymers driven by random scission, *Polym. Degrad. Stabil.* 95 (2010) 733–739, <https://doi.org/10.1016/j.polymdegradstab.2010.02.017>.
- [34] J.H. Flynn, L.A. Wall, General treatment of the thermogravimetry of polymers, *J Res Natl Bur Stand A Phys Chem* 70 (1966) 487.
- [35] T.A. Ozawa, New method of analyzing thermogravimetric data, *Bull. Chem. Soc. Jpn.* 38 (1965) 1881–1886.
- [36] K. Miura, T. Maki, A Simple Method for Estimating f(E) and K₀(E) in the Distributed Activation Energy Model, 1998.
- [37] M. Radojević, B. Janković, V. Jovanović, D. Stojiljković, N. Manić, Comparative pyrolysis kinetics of various biomasses based on model-free and DAEM approaches improved with numerical optimization procedure, *PLoS One* 13 (2018), <https://doi.org/10.1371/journal.pone.0206657>.
- [38] C.G. Mothé, I.C. de Miranda, Study of kinetic parameters of thermal decomposition of bagasse and sugarcane straw using friedman and ozawa-flynn-wall isoconversional methods, *J. Therm. Anal. Calorim.* 113 (2013) 497–505, <https://doi.org/10.1007/s10973-013-3163-7>.
- [39] M. Li, L. Jiang, J.J. He, J.H. Sun, Kinetic triplet determination and modified mechanism function construction for thermo-oxidative degradation of waste polyurethane foam using conventional methods and distributed activation energy model method, *Energy* 175 (2019) 1–13, <https://doi.org/10.1016/j.energy.2019.03.032>.
- [40] G. Özşin, A.E. Pütün, Insights into pyrolysis and Co-pyrolysis of biomass and polystyrene: thermochemical behaviors, kinetics and evolved gas analysis, *Energy Convers. Manag.* 149 (2017) 675–685, <https://doi.org/10.1016/j.enconman.2017.07.059>.

- [41] Y. Zheng, L. Tao, X. Yang, Y. Huang, C. Liu, Z. Zheng, Study of the thermal behavior, kinetics, and product characterization of biomass and low-density polyethylene Co-pyrolysis by thermogravimetric analysis and pyrolysis-GC/MS, *J. Anal. Appl. Pyrolysis* 133 (2018) 185–197.
- [42] J. Chattopadhyay, T.S. Pathak, R. Srivastava, A.C. Singh, Catalytic Co-pyrolysis of paper biomass and plastic mixtures (HDPE (high density polyethylene), PP (polypropylene) and PET (polyethylene terephthalate)) and product analysis, *Energy* 103 (2016) 513–521, <https://doi.org/10.1016/j.energy.2016.03.015>.
- [43] Z. Alhulaybi, I. Dubdub, M. Al-Yaari, A. Almithn, A.F. Al-Naim, H. Aljanubi, Pyrolysis kinetic study of polylactic acid, *Polymers* 15 (2023), <https://doi.org/10.3390/polym15010012>.
- [44] L. Jiang, X.R. Yang, X. Gao, Q. Xu, O. Das, J.H. Sun, M.K. Kuzman, Pyrolytic kinetics of polystyrene particle in nitrogen atmosphere: particle size effects and application of distributed activation energy method, *Polymers* 12 (2020), <https://doi.org/10.3390/polym12020421>.
- [45] J.D.S. Castro, E.G.P. da Silva, C.F. Virgens, Evaluation of models to predict the influence of chemical pretreatment on the peels of *nephelium lappaceum* L. Based on pyrolysis kinetic parameters obtained using a combined fraser-suzuki function and friedman's isoconversional method, *J. Anal. Appl. Pyrolysis* 149 (2020), 104827, <https://doi.org/10.1016/j.jaap.2020.104827>.
- [46] B.D. Bárbara, N.R.S. Araújo, R.F. Ligório, F.J.P. Pujatti, M.I. Yoshida, R.C. O. Sebastião, Comparative kinetic study of automotive polyurethane degradation in non-isothermal and isothermal conditions using artificial neural network, *Thermochim Acta* 666 (2018) 116–123, <https://doi.org/10.1016/j.tca.2018.06.014>.
- [47] L. Jiang, H.H. Xiao, J.J. He, Q. Sun, L. Gong, J.H. Sun, Application of genetic algorithm to pyrolysis of typical polymers, *Fuel Processing Technology* 138 (2015) 48–55, <https://doi.org/10.1016/j.fuproc.2015.05.001>.
- [48] I. Dubdub, Pyrolysis study of mixed polymers for non-isothermal TGA: artificial neural networks application, *Polymers (Basel)* 14 (2022), <https://doi.org/10.3390/polym14132638>.
- [49] S. Armenise, S. Wong, J.M. Ramírez-Velásquez, F. Launay, D. Wuebben, B. B. Nyakuma, J. Rams, M. Muñoz, Application of computational approach in plastic pyrolysis kinetic modelling: a review, *Reaction Kinetics, Mechanisms and Catalysis* 134 (2021) 591–614.
- [50] S.S. Lins, C.F. Virgens, W.N.L. dos Santos, I.H.S. Estevam, G.C. Brandão, C.S. A. Felix, S.L.C. Ferreira, On-line solid phase extraction system using an ion imprinted polymer based on dithizone chelating for selective preconcentration and determination of mercury(II) in natural waters by CV AFS, *Microchemical Journal* 150 (2019), 104075, <https://doi.org/10.1016/j.microc.2019.104075>.
- [51] A. Brems, J. Baeyens, J. Beerlandt, R. Dewil, Thermogravimetric pyrolysis of waste polyethylene-terephthalate and polystyrene: a critical assessment of kinetics modelling, *Resour Conserv Recycl* 55 (2011) 772–781, <https://doi.org/10.1016/j.resconrec.2011.03.003>.
- [52] V. Mortezaeikia, O. Tavakoli, M.S. Khodaparasti, A review on kinetic study approach for pyrolysis of plastic wastes using thermogravimetric analysis, *J Anal Appl Pyrolysis* 160 (2021), 105340, <https://doi.org/10.1016/j.jaap.2021.105340>.
- [53] C.B. Felix, W.H. Chen, A.T. Ubando, Y.K. Park, K.Y.A. Lin, A. Pugazhendhi, T. B. Nguyen, C. Dong, A. di, Comprehensive review of thermogravimetric analysis in lignocellulosic and algal biomass gasification, *Chemical Engineering Journal* 445 (2022), 136730, <https://doi.org/10.1016/j.cej.2022.136730>.
- [54] T. Wanjuan, W. Cunxin, C. Donghua, Kinetic studies on the pyrolysis of chitin and chitosan, *Polym Degrad Stab* 87 (2005) 389–394, <https://doi.org/10.1016/J.POLYMEDEGRADSTAB.2004.08.006>.
- [55] P. Qiao, Z. Guo, Y. Zhang, J. Li, W. Zhang, M. Liu, Comparative study on pyrolysis kinetics of agroforestry biomass based on distributed activation energy model method, *Journal of Fuel Chemistry and Technology* 50 (2022) 808–823, [https://doi.org/10.1016/S1872-5813\(21\)60009-4](https://doi.org/10.1016/S1872-5813(21)60009-4).
- [56] C.D. Doyle, Estimating isothermal life from thermogravimetric data, *J Appl Polym Sci* 6 (1962) 639–642.
- [57] J. Demsar, B. Zupan, G. Leban, T. Curk, Orange : from experimental machine learning, *Knowledge Discovery in Databases: PKDD 2004* (2004) 537–539, https://doi.org/10.1007/978-3-540-30116-5_58.
- [58] V. Vapnik, *The Nature of Statistical Learning Theory*, Springer science & business media, 2013. ISBN 1475732643.
- [59] J. Luts, F. Ojeda, R. van de Plas Raf, B. de Moor, S. van Huffel, J.A.K. Suykens, A tutorial on support vector machine-based methods for classification problems in chemometrics, *Anal Chim Acta* 665 (2010) 129–145, <https://doi.org/10.1016/j.aca.2010.03.030>.
- [60] Y. Freund, R.E. Schapire, Experiments with a new boosting algorithm, in: *Proceedings of the Icml*; Citeseer, vol. 96, 1996, pp. 148–156.
- [61] R. Tibshirani, *Regression Shrinkage and Selection via the Lasso*, vol. 58, 1996.
- [62] V.N. Gudivada, M.T. Irfan, E. Fathi, D.L. Rao, *Cognitive analytics: going beyond big data analytics and machine learning*, in: *Handbook of Statistics*, vol. 35, Elsevier B. V., 2016, pp. 169–205. ISBN 9780444637444.
- [63] Susmaga, R. *Confusion Matrix Visualization*;
- [64] J. Demsar, T. Curk, A. Erjavec, C. Gorup, T. Hocevar, M. Milutinovic, M. Možina, M. Polajnar, M. Toplak, A. Staric, et al., *Orange: Data Mining Toolbox in Python*, vol. 14, 2013.
- [65] J.M. Criado, J. Málek, A. Ortega, Applicability of the master plots in kinetic analysis of non-isothermal data, *Thermochim Acta* 147 (1989) 377–385, [https://doi.org/10.1016/0040-6031\(89\)85192-5](https://doi.org/10.1016/0040-6031(89)85192-5).
- [66] L.A. Pérez-Maqueda, C. Popescu, S. Vyazovkin, A.K. Burnham, N. Sbirrazzuoli, J. M. Criado, ICTAC kinetics committee recommendations for performing kinetic computations on thermal analysis data, *Thermochim Acta* 520 (2011) 1–19, <https://doi.org/10.1016/j.tca.2011.03.034>.
- [67] L.A. Pérez-Maqueda, J.M. Criado, Accuracy of Senum and yang's approximations to the Arrhenius integral, *J Therm Anal Calorim* 60 (2000) 909–915, <https://doi.org/10.1023/A:1010115926340>.
- [68] M. Poletto, A.J. Zattera, R.M.C. Santana, Thermal decomposition of wood: kinetics and degradation mechanisms, *Bioresour Technol* 126 (2012) 7–12, <https://doi.org/10.1016/j.biortech.2012.08.133>.
- [69] National Institute of Advanced Industrial Science and Technology (AIST) *Infrared Spectra of Methacrylic Acid*; SDBS No.: 1222..
- [70] O. Planinšek, D. Planinšek, A. Zega, M. Breznik, S. Srčić, Surface analysis of powder binary mixtures with ATR FTIR spectroscopy, *Int J Pharm* 319 (2006) 13–19, <https://doi.org/10.1016/J.IJPHARM.2006.03.048>.
- [71] L.F.C. Miranda, D.S. Domingues, M.E.C. Queiroz, Selective solid-phase extraction using molecularly imprinted polymers for analysis of venlafaxine, O-desmethylvenlafaxine, and N-desmethylvenlafaxine in plasma samples by liquid chromatography–tandem mass spectrometry, *J Chromatogr A* 1458 (2016) 46–53, <https://doi.org/10.1016/j.chroma.2016.06.024>.
- [72] S.M.F. Langeroodi, M. Kazempour, T. Eslaminejad, A. Naghipour, M. Ansari, Molecular imprinted polymer with dorzolamide for contact lens applications assisted by computational and experimental design, *React Funct Polym* 178 (2022), 105355, <https://doi.org/10.1016/j.reactfunctpolym.2022.105355>.
- [73] H.G. Brittain, R.D. Bruce, Chapter 4 thermal analysis, *Comprehensive Analytical Chemistry* 47 (2006) 63–109, [https://doi.org/10.1016/S0166-526X\(06\)47004-5](https://doi.org/10.1016/S0166-526X(06)47004-5).
- [74] C.G. Mothé, A.D. Azevedo, *de Análise Térmica de Materiais*, São Paulo, Artiber, 2009.
- [75] D. Dollimore, S. Lerdkanchanaporn, Thermal analysis, *Anal Chem* 70 (1998) 4936–4949, <https://doi.org/10.1021/a19800038>.
- [76] R. Xiao, W. Yang, Influence of temperature on organic structure of biomass pyrolysis products, *Renew Energy* 50 (2013) 136–141, <https://doi.org/10.1016/j.renene.2012.06.028>.
- [77] W.G. Hanna, M.A. Mekewi, E.-S.H. El-Mosallamy, Dithizone and carbazone complex compounds as initiators and γ -radiation anti-degradation agents for poly (methyl methacrylate), *International Journal of Polymeric Materials and Polymeric Biomaterials* 52 (2003) 471–483, <https://doi.org/10.1080/009140303004911>.
- [78] L. Fan, Y. Zhang, S. Liu, N. Zhou, P. Chen, Y. Cheng, M. Addy, Q. Lu, M.M. Omar, Y. Liu, et al., Bio-oil from Fast pyrolysis of lignin: effects of process and upgrading parameters, *Bioresour Technol* 241 (2017) 1118–1126, <https://doi.org/10.1016/j.biortech.2017.05.129>.
- [79] A. Bhavanam, R.C. Sastry, Kinetic study of solid waste pyrolysis using distributed activation energy model, *Bioresour Technol* 178 (2015) 126–131, <https://doi.org/10.1016/J.BIORTECH.2014.10.028>.
- [80] S. Abbasi, M. Roushani, H. Khani, R. Sahraei, G. Mansouri, Synthesis and application of ion-imprinted polymer nanoparticles for the determination of nickel ions, *Spectrochim Acta A Mol Biomol Spectrosc* 140 (2015) 534–543, <https://doi.org/10.1016/J.SAA.2014.11.107>.
- [81] P. Budrugaec, A. Cucos, R. Dascălu, I. Atkinson, P. Osiceanu, Application of model-free and multivariate nonlinear regression methods for evaluation of the kinetic scheme and kinetic parameters of thermal decomposition of low density polyethylene, *Thermochim Acta* (2022) 708, <https://doi.org/10.1016/j.tca.2021.179138>.
- [82] S. Yousef, J. Eimontas, N. Striugas, A. Mohamed, M. Ali Abdelnaby, Pyrolysis kinetic behavior and TG-FTIR-GC-MS analysis of end-life ultrafiltration polymer nanocomposite membranes, *Chemical Engineering Journal* 428 (2022), 131181, <https://doi.org/10.1016/J.CEJ.2021.131181>.
- [83] J.D.S. Castro, C.F. das Virgens, Thermal decomposition of *nephelium lappaceum* L. Peel, *J Therm Anal Calorim* 138 (2019) 3541–3549, <https://doi.org/10.1007/s10973-019-08289-3>.
- [84] D. Ballabio, F. Grisoni, R. Todeschini, Multivariate comparison of classification performance measures, *Chemometrics and Intelligent Laboratory Systems* 174 (2018) 33–44, <https://doi.org/10.1016/j.chemolab.2017.12.004>.
- [85] R.E. Schapire, *Explaining Adaboost, Empirical Inference: Festschrift in Honor of Vladimir N. Vapnik* (2013) 37–52.
- [86] D.M. Hawkins, The problem of overfitting, *J Chem Inf Comput Sci* 44 (2004) 1–12.
- [87] P. Refaailzadeh, L. Tang, H. Liu, Cross-validation, *Encyclopedia of database systems* 5 (2009) 532–538.
- [88] S.M. Abd Elrahman, A. Abraham, *A Review of Class Imbalance Problem* 1 (2013).
- [89] J. Cai, W. Wu, R. Liu, An overview of distributed activation energy model and its application in the pyrolysis of lignocellulosic biomass, *Renewable and Sustainable Energy Reviews* 36 (2014) 236–246.
- [90] A. Khawam, D.R. Flanagan, Solid-state kinetic models: basics and mathematical fundamentals, *Journal of Physical Chemistry B* 110 (2006) 17315–17328, <https://doi.org/10.1021/jp062746a>.
- [91] Chapter 3 kinetic models for solid state reactions, in: A.K. Galwey, M.E. Brown (Eds.), *Studies in Physical and Theoretical Chemistry* vol. 86, Elsevier, 1999, pp. 75–115. ISBN 0167-6881.
- [92] P. Das, P. Tiwari, Thermal degradation kinetics of plastics and model selection, *Thermochim Acta* 654 (2017) 191–202, <https://doi.org/10.1016/j.tca.2017.06.001>.